Improved strength and interfacial microstructure of dissimilar Al/steel weld via combined addition of Zn and Ni

Kiyoaki T Suzuki, Shun Omura, Shun Tokita, Yujiro Tatsumi, Sylvain Dancette, Yutaka S Sato

Materials & Design 245 (2024) 113302

Contents lists available at ScienceDirect

Materials & Design

journal homepage: www.elsevier.com/locate/matdes

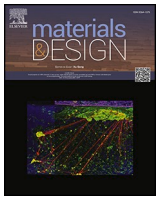

Improved strength and interfacial microstructure of dissimilar Al/steel weld via combined addition of Zn and Ni

Kiyoaki T. Suzuki [a,*], Shun Omura [a], Shun Tokita [a], Yujiro Tatsumi [b], Sylvain Dancette [c], Yutaka S. Sato [a,c]

[a] Department of Materials Processing, Graduate School of Engineering, Tohoku University, 6-6-02 Aramaki-aza-Aoba, Aoba-ku, Sendai, Miyagi 980-8579, Japan
[b] Nippon Steel Corporation, 20-1 Shintomi, Futtsu, Chiba 293-8511, Japan
[c] ELyTMaX IRL3757, CNRS, Univ Lyon, INSA Lyon, Centrale Lyon, Université Claude Bernard Lyon 1, Tohoku University, Sendai, Miyagi 980-8577, Japan

ARTICLE INFO

Keywords:
Welding
Aluminum alloy
Steel
Intermetallic compounds
Microstructure

ABSTRACT

The effect of the combined addition of Zn and Ni on the mechanical properties and microstructures of an intermetallic compound (IMC) layer of dissimilar welds of Al alloy 5052 to low-carbon steel was systematically investigated. A maximum weld strength of 120 MPa was achieved with the combined addition of Zn and Ni, which was 193 % higher than that of the weld produced without the addition of Zn or Ni. The addition of Zn resulted in the formation of soft Fe–Zn IMCs in the IMC layer, which reduced the hardness of the IMC layer. Additionally, the combined addition of Zn and Ni promoted the formation of Fe–Zn IMCs, which further softened the IMC layer. Further softening of the IMC layer, reduction in the thickness of the IMC layer, and suppression of the formation of defects in the IMC layer, achieved by the combined addition of Zn and Ni, drastically improved the weld strength.

1. Introduction

Global initiatives to reduce CO_2 emissions emphasize the urgent need for climate action, prompting the automotive industry to focus on reducing vehicle weight as a vital strategy. The integration of Al and steel in multi-material vehicle structures is highly anticipated because of their potential to balance weight reduction with enhanced collision safety [1–3]. However, the dissimilar welding of Al alloys to steel remains a significant challenge, primarily owing to the formation of brittle intermetallic compound (IMC) layers. Numerous studies show that thick η-Fe_2Al_5 and thin θ-Fe_4Al_{13} layers are formed at the weld interface [4–8]. These intrinsically brittle IMCs significantly deteriorate the strength of Al/steel welds [9–11]. To improve weld strength, it is crucial to understand and control the formation of IMC layers. The formation and growth of IMC layers are influenced by the thermal history of the welding process and chemical composition of the utilized materials.

Reducing the thickness of the IMC layer increases Al/steel weld strength [12–14]. Thus, most studies have focused on applying low-heat-input welding processes for welding Al to steel. They primarily aimed to optimize the welding conditions to minimize the growth of the IMC layers, thereby enhancing the weld performance. Fusion welding techniques, such as brazing with arc [15–17] or laser [18–20] heat sources, and solid-state welding processes, such as friction stir welding (FSW) [21–23], friction stir spot welding (FSSW) [24,25], and ultrasonic welding (USW) [26–28], can effectively reduce the heat input during welding, reduce the IMC thickness, and improve weld strength. However, to achieve the optimal IMC layer thickness range for high-strength welds, precise control of the welding process is necessary.

The addition of alloying elements is effective in controlling the microstructure of the IMC layer. The impact of Si addition has been well established: Si significantly reduces the thickness of the IMC layer formed at the Al/steel weld interface [29–34], resulting in an improvement in the weld strength [35,36]. Cheng et al. [37] highlighted that the formed Al–Fe–Si IMCs (τ_1-$Al_2Fe_3Si_3$ and τ_5-Al_7Fe_2Si) acted as a diffusion barrier of Al atoms and the occupation of vacancies in η-Fe_2Al_5 by Si atoms reduced atomic mobility, thus inhibiting growth of the IMC layer. Furuya et al. [38] conducted gas tungsten arc welding (GTAW) of Al alloys containing Ni, Cr, Ti, and Mn individually to steel and examined the effect of these alloying elements on the weld strength. They suggested that the grain size of η-Fe_2Al_5 affected the weld strength, rather than the thickness of the IMC layer, and reported that grain refinement of η-Fe_2Al_5 due to Ni addition improved the weld strength

* Corresponding author.
E-mail address: kiyoaki.suzuki.q1@dc.tohoku.ac.jp (K.T. Suzuki).

https://doi.org/10.1016/j.matdes.2024.113302
Received 21 July 2024; Received in revised form 25 August 2024; Accepted 6 September 2024
Available online 8 September 2024

Table 1
Chemical compositions of the base materials used in the present study (wt.%).

	Fe	C	Si	Mn	P	S	Al	Cu	Mg	Cr	Zn
LCS	Bal.	0.003	–	0.35	0.020	0.008	–	–	–	–	–
AA5052	0.25	–	0.08	0.01	–	–	Bal.	0.01	2.61	0.17	0.02

most effectively. Suzuki et al. [39] reported a significant improvement in the strength of Al/steel welds with the addition of Si and Ni. The combined Si and Ni addition achieved both the thinning of the IMC layer via Si addition and the refinement of η-Fe_2Al_5 grains via Ni addition simultaneously, significantly improving the weld strength. This study also demonstrated the potential for further improvements in the strength of Al/steel welds through the combined addition of multiple alloying elements.

The effect of Zn on Al/steel welding is also critical because Zn coatings on steel surfaces have been widely used. Recently, it was reported that the addition of Zn to an Al/steel weld interface reduced the hardness of the IMC layer, thereby improving the weld strength. Qin et al. [40] joined AA5052 to galvanized steel by gas metal arc welding in a lap configuration and reported that the formation of η-$Fe_2Al_5Zn_{0.4}$ in the IMC layer was the main factor for improving the fracture toughness of the weld. Conversely, Yang et al. [41] produced AA5754/DP980 steel welds by laser welding with a Zn–Al filler material and examined the effect of Zn on the microstructure of the IMC layer and the mechanical properties of the weld. They found that η-$Fe_2Al_{5-x}Zn_x$ was harder than η-Fe_2Al_5 but the formation of the much softer $FeZn_{10}$ contributed to the improvement in the weld strength. Ma et al. [42] conducted a transmission electron microscopy (TEM) analysis of the weld interface of AA5083 to FH36 steel produced by GTAW with a Zn–Al filler wire. They reported that η-$Fe_2Al_5Zn_{0.4}$, δ-$FeZn_{10}$, and Γ-Fe_3Zn_{10} were formed at the weld interface and η/δ and η/Γ obeyed each specific orientation relationship. Although a unified understanding of the IMC softening mechanism via Zn addition is still lacking, numerous studies have reported that Zn reduces the hardness of the IMC layer, thereby improving the Al/steel weld strength. This implies that further improvement in the Al/steel weld strength can be achieved through the combined addition of Zn and other elements, such as Ni.

Thus, the primary aim of this study is to explore the potential for improving Al/steel weld strength through the combined addition of Zn and Ni. In this study, AA5052 and low-carbon steel (LCS) sheets were welded using a GTAW-based brazing process incorporating a combination of an Al–Zn filler and Ni plating. This approach enables the combined addition of alloying elements at the weld interface. In this study, the welds produced using the Al–xZn filler with and without Ni plating are denoted as xZn and xZn–Ni welds, respectively. The effects of Zn and Ni on the weld strength and microstructure of the IMC layers were comprehensively examined. Additionally, detailed microstructural analyses of the IMC layers were performed using various electron microscopes to elucidate the softening mechanisms of the IMC layers and provide fundamental ways to further improve the Al/steel weld strength.

2. Experimental procedures

In this study, LCS sheets with dimensions of 100 mm × 60 mm × 2 mm and AA5052 sheets with dimensions of 100 mm × 50 mm × 2 mm were utilized as the base materials. The chemical compositions of the base materials are listed in Table 1. The base materials were welded using GTAW-based brazing. To appropriately add Zn and Ni to the weld interface during the welding process, an Al–Zn filler combined with Ni plating on the steel surface was used for brazing. Al–Zn alloys with Zn contents of 0, 1, 3, and 5 at. % were cast, heat-treated to eliminate casting segregation, and then rolled down. Finally, they were cut into rods with dimensions of 100 mm × 5 mm × 2 mm, which served as the filler materials. Ni plating was applied to the steel surface via electroplating. The thickness of the Ni plating was approximately 19 μm, selected based on our previous work [39], where Ni plating with the thickness of approximately 28 μm did not completely dissolve in the Al fusion zone.

Fig. 1**a** illustrates a schematic of the brazing process. Before brazing, the surfaces of both the AA5052 and Al–Zn filler were ground using SiC sandpaper to remove oxide films and then cleaned with acetone. The steel sheets were then cleaned with acetone. Flux was applied to enhance the weldability. AA5052 and the Al–Zn filler were placed on a steel sheet with an overlap width of 25 mm and secured to a welding jig with screws. The tungsten electrode was positioned 4 mm towards the Al side from the edge of the Al–Zn filler, primarily directing the arc onto the Al side to achieve Al/steel brazing without steel melting. The brazing parameters included an arc current of 140 A, voltage of 9 V, speed of 200 mm/min, arc length of 1 mm, and a tilt angle of 10° from the horizontal to improve the wetting angle. Brazing was performed in an argon atmosphere to prevent oxidation, supplemented with an argon shielding gas at a flow rate of 20 L/min. Note that the brazing parameters were selected based on preliminary brazing experiments to achieve a defect-free weld appearance. Tensile shear tests were conducted to examine the weld strength. Test specimens, 10 mm in width, were extracted from the center of each weld using electrical discharge machining (EDM), as shown in Fig. 1**b**. Three samples of each weld were tested to determine the average weld strength. As shown in Fig. 1**c**, before the tests, two slits were introduced into each test specimen using EDM to limit the test area to 20 mm^2. The tests were performed using an Instron-type testing machine at a crosshead speed of 0.3 mm/min at room temperature (298 K). After the tests, X-ray diffraction (XRD) was performed on the fracture surfaces to identify the fracture locations. For

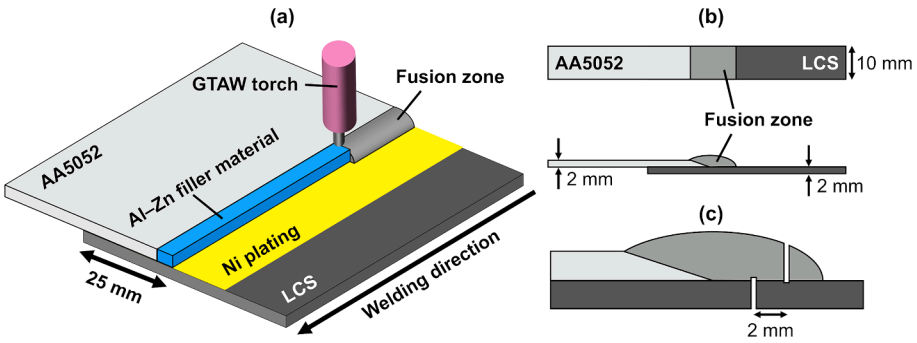

Fig. 1. Schematics of (a) the GTAW-based brazing process, (b) dimension of a tensile shear test specimen, and (c) location of slits.

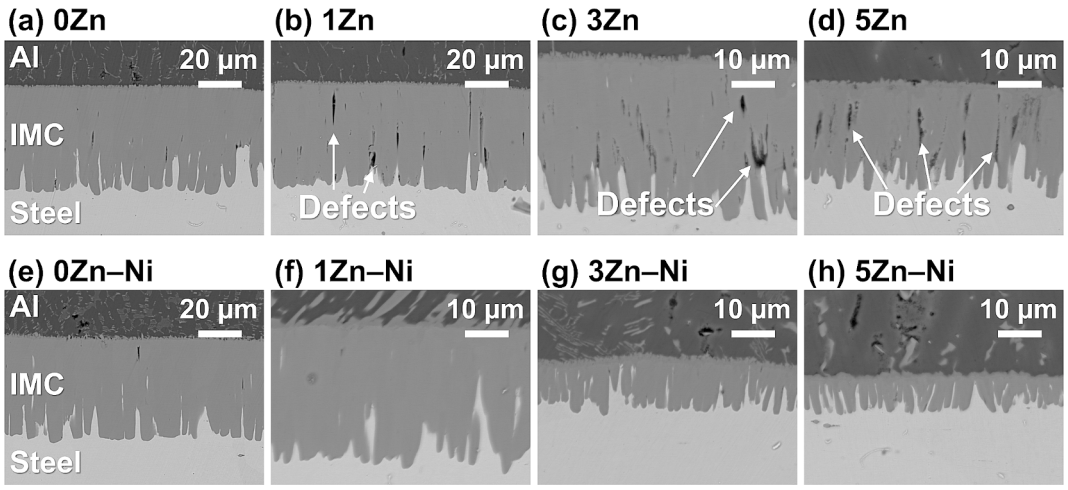

Fig. 2. BSE images of the different Al/steel weld interfaces of welds produced using Al–Zn filler with different Zn content of 0–5 at.% (a–d) without and (e–h) with Ni plating. The white arrows in **b–d** indicate defects formed in the intermetallic compounds (IMC) layer.

microstructural analysis and nanoindentation tests, specimens with a width of 2 mm were cut from the weld center using EDM. The cross sections were polished initially with SiC sandpapers, with a 1 μm diamond suspension, and then with a colloidal silica solution. The polished cross sections were examined using a scanning electron microscope (SEM) in backscattered electron (BSE) mode to measure the thickness of the IMC layers. Chemical composition analyses were performed using wavelength and energy dispersive spectroscopy (WDS and EDS, respectively) combined with SEM. Additionally, electron backscatter diffraction (EBSD) was used to observe the grain morphology of the IMC formed at the weld interface. Cross-sectional TEM samples, approximately 10 μm in width, were extracted from both the Al/IMC interface and inner IMC layer, and subsequently thinned using a focused ion beam (FIB) system. The IMCs formed at the weld interface were identified using EDS and selected area electron diffraction (SAED) patterns. The hardness of the IMC layer was examined by nanoindentation tests using a Berkovich indenter at a maximum load of 20 mN. The hardness data were taken at ten random points in the η-Fe_2Al_5 layer, calculating the average value.

3. Results and discussion

3.1. Microstructure of weld interface

Fig. 2 shows the BSE images of the weld interfaces. Note that this figure includes images captured at different magnifications. Regardless of the utilization of Ni plating in the brazing process, an IMC layer was formed at all weld interfaces. The Ni plating dissolved in the Al melts during the brazing process, resulting in a liquid Al/solid Fe reaction. All welds show a distinctive "tongue-like" structure at the IMC/steel interface, which is consistent with previous studies on the liquid-Al/solid-Fe interface [43,44]. Furthermore, SEM-WDS measurements were performed at five different points in the central area of the IMC layer for several representative welds. The SEM-WDS results revealed that the average chemical composition of the IMC layers was 28.0 at.% Al-72.0 at.% Fe for the 0Zn weld, 26.8 at.% Al-72.9 at.% Fe-0.2 at.% Zn for the 3Zn weld, and 26.8 at.% Al-72.8 at.% Fe-0.3 at.% Zn for the 3Zn–Ni weld. These chemical compositions, coupled with the distinct "tongue-like" morphology, indicated that a thick η-Fe_2Al_5 layer was formed at the weld interfaces. Moreover, the SEM-WDS analysis indicated that only Zn was dissolved into the η-Fe_2Al_5 layer, although Ni and Mg contained in AA5052 were also in the Al melt during brazing. Additionally, BSE images exhibit the void-like defects in the η-Fe_2Al_5 layer of the weld produced using Al–Zn filler without Ni plating (1Zn, 3Zn, and 5Zn welds), and the area fraction of the defects increases with increasing the Zn content of the filler. In contrast, the welds produced by Ni plating (1Zn–Ni, 3Zn–Ni, and 5Zn–Ni welds) hardly exhibited defects in the η-Fe_2Al_5 layer. These defects in the η-Fe_2Al_5 layer might deteriorate the weld strength, which will be discussed later. Fig. 3 displays the bright field-scanning transmission electron microscopy (BF-STEM) images taken from the Al/IMC interface of the 3Zn and 3Zn–Ni welds (Fig. 3**a and b**) and SAED patterns (Fig. 3**c**). In both welds, a thin layer of

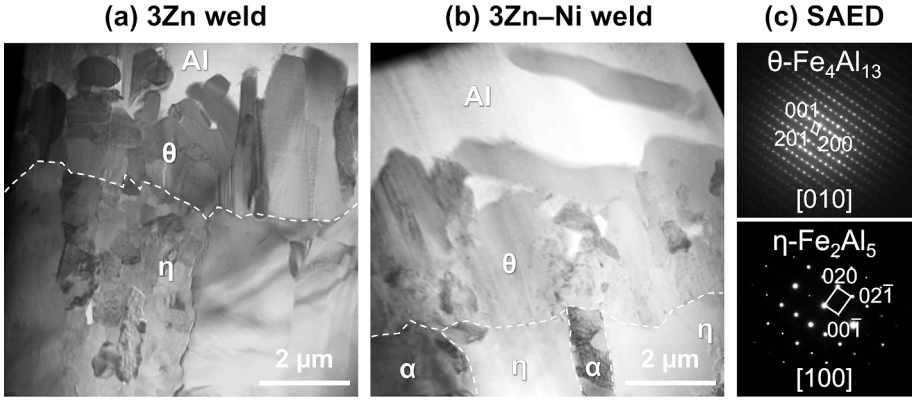

Fig. 3. BF-TEM images of the Al/IMC interface of the (a) 3Zn and (b) 3Zn–Ni welds. The white dash lines in a and b indicate the phase boundaries. (c) SAED patterns of θ-Fe_4Al_{13} and η-Fe_2Al_5. The zone axis of SAED patterns is given at the bottom of each image.

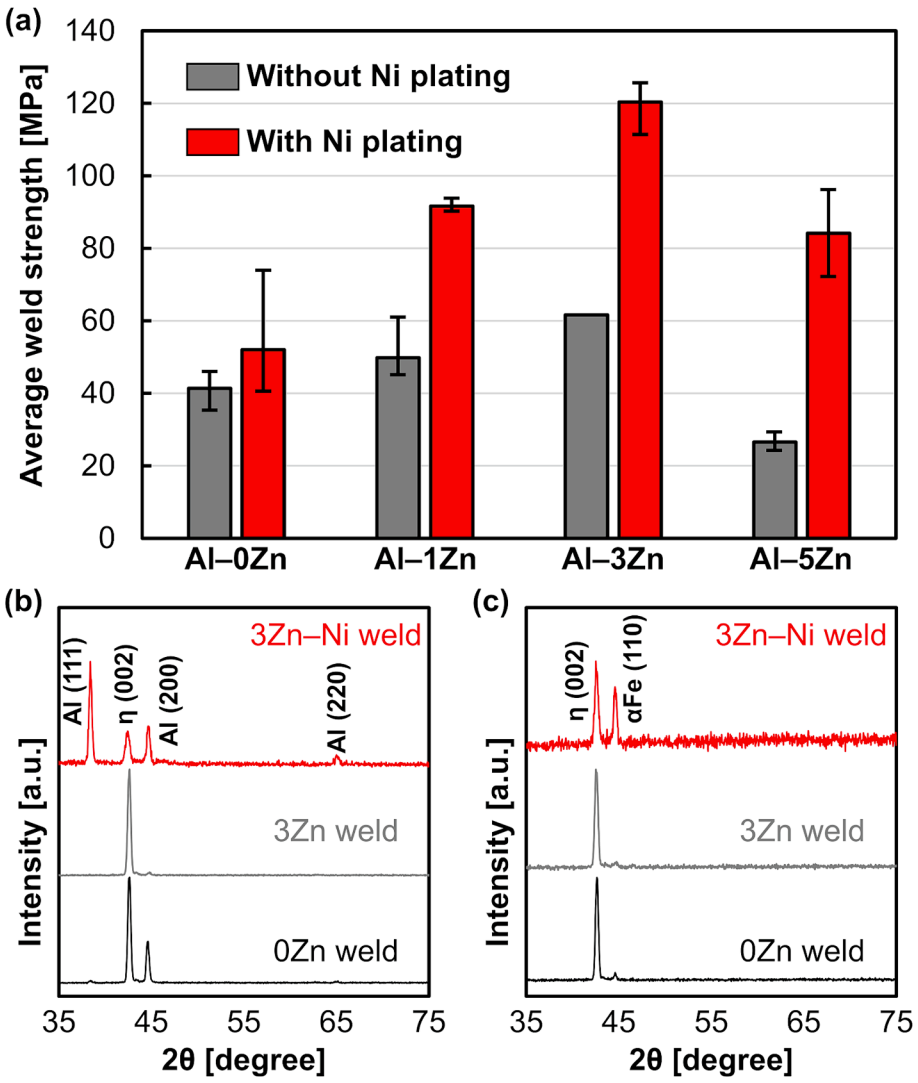

Fig. 4. (a) Average weld strength of each weld. XRD spectra obtained from the fracture surfaces of the (b) Al and (c) steel sides of the 0Zn (black line), 3Zn (grey line), and 3Zn–Ni (red line) welds. Diffraction peaks are indexed by η-Fe_2Al_5, bcc (Fe), or fcc (Al).

θ-Fe_4Al_{13} (monoclinic, C2/m, a = 15.509 Å, b = 8.066 Å, c = 12.469 Å, β = 107.72° [45]) is formed, in addition to the thick η-Fe_2Al_5 (orthorhombic, Cmcm, a = 7.584 Å, b = 6.4094 Å, c = 4.213 Å [46]). The θ-Fe_4Al_{13} is typical sub-layer formed adjacent to the η-Fe_2Al_5 layer.

3.2. Weld strength and fracture location

Fig. 4**a** shows the average strength of each weld. The error bars in the figure indicate the minimum and the maximum values. It should be noted that all the specimens fractured at the weld interface in a brittle manner. In welds without any alloying elements (0Zn weld), the weld strength was low at only 41 MPa. Without Ni plating, increasing the Zn content of the filler initially increased the weld strength up to 3Zn weld, with a weld strength of 62 MPa. However, the 5Zn weld exhibited a low weld strength compared to that of the 0Zn weld. When Ni plating was used with the Al–Zn filler, the relationship between the Zn content of the filler and weld strength remained consistent; however, the weld strength was always higher than when the Al–Zn filler was used alone. A maximum weld strength of 120 MPa was achieved for the 3Zn–Ni weld. This result highlights that the combined addition of Zn and Ni significantly improves the Al/steel weld strength. The mechanisms of the strengthening the weld will be examined in terms of the microstructural change in the IMC layer.

To identify the fracture locations, XRD was applied to the fracture surfaces after the tensile shear tests. Fig. 4**b and c** show the XRD spectra obtained from the fracture surfaces of the 0Zn, 3Zn, and 3Zn–Ni welds. The peak of η-Fe_2Al_5 is observed in all spectra of both Al (Fig. 4**b**) and steel (Fig. 4**c**) sides, indicating that fractures occurred in the η-Fe_2Al_5 layer during the tensile shear tests. This result emphasizes the importance of the properties of the η-Fe_2Al_5 layer for the weld strength.

Fig. 5**a** presents a secondary electron (SE) image of a fracture surface taken from the steel side of a weld produced using an Al–Zn filler with high Zn content. The fracture surface represents a brittle fracture in the η-Fe_2Al_5 layer. In addition, several voids were observed on the fractured surface. The EDS maps (Fig. 5**b**) show that Zn was enriched at the periphery of these voids, as indicated by the white arrows, suggesting that the Zn dissolved in the η-Fe_2Al_5 layer could cause the formation of voids. In addition, we confirmed that the number of voids increased with increasing Zn content in the filler used for brazing. This trend in the number of voids was in good agreement with that observed in the cross sections of the welds (Fig. 2). Because of the low boiling temperature of Zn (906 °C) [47], Zn dissolved in η-Fe_2Al_5 layer would evaporate during the brazing process, resulting in the formation of the voids. Therefore, the relatively low weld strengths of the 5Zn and 5Zn–Ni welds (Fig. 4**a**) arose from the massive formation of these voids. As aforementioned, using Ni plating combined with an Al–Zn filler can suppress the

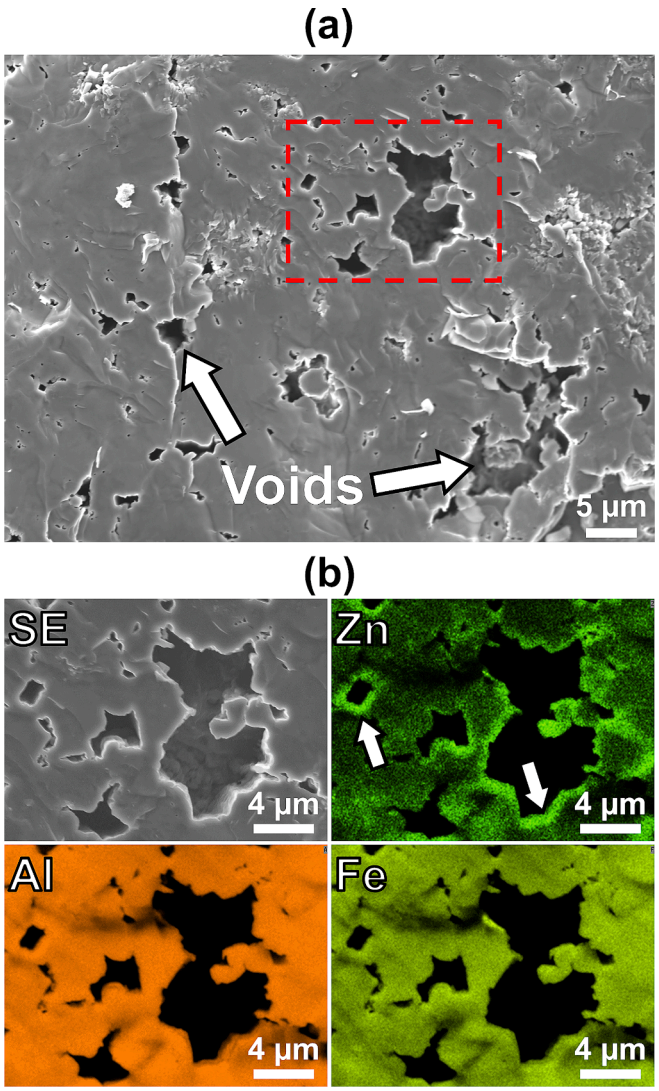

Fig. 5. (a) SE image of a fracture surface taken from the steel side of a weld produced using an Al–Zn filler without Ni plating. The white arrows in **a** indicate the voids formed in the fracture surface. (b) Enlarged SE image and corresponding EDS maps of the area highlighted by the red rectangle in **a**. The white arrows in Zn maps indicate the Zn enrichment at the periphery of the voids.

formation of voids, which might contribute to an improvement in the weld strength.

3.3. Thickness of IMC layer

Numerous studies have shown a correlation between the thickness of the IMC layer and strength of Al/steel welds: a thinner IMC layer results in a higher weld strength [12–14]. Accordingly, this study also examined the thickness of the IMC layer and its effect on weld strength. Fig. 6**a** shows the thickness of the IMC layer of each weld. The error bars indicate the standard deviation of the IMC thickness measured from several BSE images. Except for the 1Zn and 0Zn–Ni welds, the addition of Zn and Ni decreased the thicknesses of the IMC layers. Each alloying element, Zn, Ni, and Mg, may change the temperature of the Al melt by varying the reaction temperature and time between the liquid Al and solid Fe, resulting in different microstructures of the IMC layer. Additionally, the Ni plating prevented direct contact between the liquid Al and steel during the initial stage of the brazing process, thereby suppressing the growth of the IMC layer. These findings indicate that understanding the effects of alloying elements on the formation and growth of the IMC layer requires the consideration of both the addition process and experimental measurements of the temperature history at the weld interface, as well as numerical simulations. These studies are ongoing and will be reported in separate papers in the future. Fig. 6**b** shows the relationship between the weld strength and thickness of the IMC layer. Except for the 5Zn and 5Zn–Ni welds, the weld strength increases with decreasing IMC layer thickness. The relatively lower weld strength of the 5Zn and 5Zn–Ni welds was due to a high number of voids in the η-Fe_2Al_5 layer, as previously discussed. The trend of high weld strength with the thickness of the IMC layer is in good agreement with previous studies [12–14]. In general, however, they reported that the thickness of the IMC layer should be less than 10 μm to avoid the degradation of the Al/steel weld strength [48–51]. Thus, the significant improvement in weld strength by the combined addition of Zn and Ni cannot be explained only by the thinning of the IMC layer. To further elucidate the mechanisms of the improvement in weld strength, additional analyses were conducted, primarily focusing on the 0Zn, 3Zn, and 3Zn–Ni welds.

3.4. Hardness of IMC layer and its softening mechanism

In this study, a nanoindentation test of the IMC layer was conducted, showing that the average hardness values of the IMC layer in the 0Zn, 3Zn, and 3Zn–Ni welds were 7.1 ± 0.5 GPa, 5.7 ± 0.4 GPa, and 4.1 ± 0.3 GPa, respectively. This result verified not only the reduction in the hardness of the IMC layer by Zn addition [40–42] but also the further softening of the IMC layer by the combined addition of Zn and Ni. This further softening of the IMC layer contributed to an improvement in the

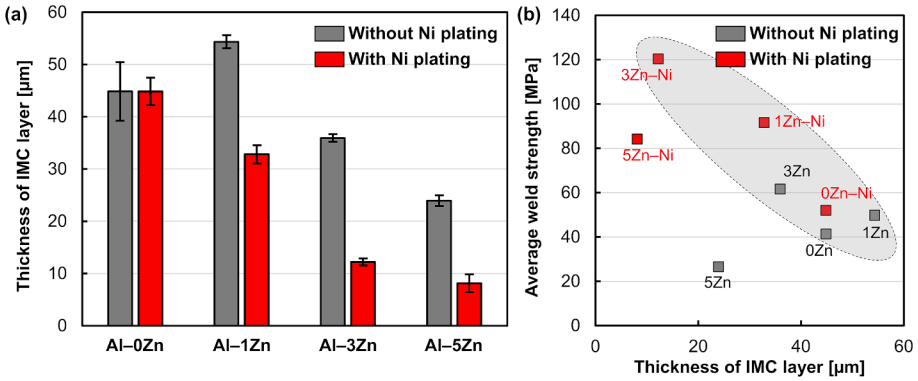

Fig. 6. (a) Thickness of the IMC layer formed at the different Al/steel weld interfaces. (b) Relationship between the thickness of the IMC layer and average weld strength.

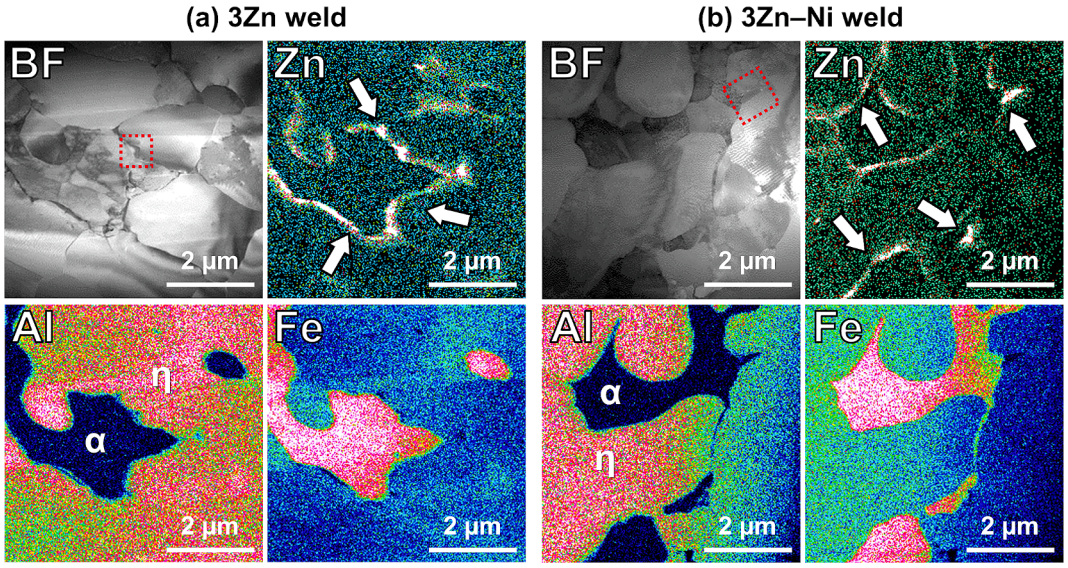

Fig. 7. STEM-EDS maps of the IMC layer of the (a) 3Zn and (b) 3Zn–Ni welds. The white arrows in each Zn map indicates the Zn enrichment along the interface between η-Fe_2Al_5 and α-Fe.

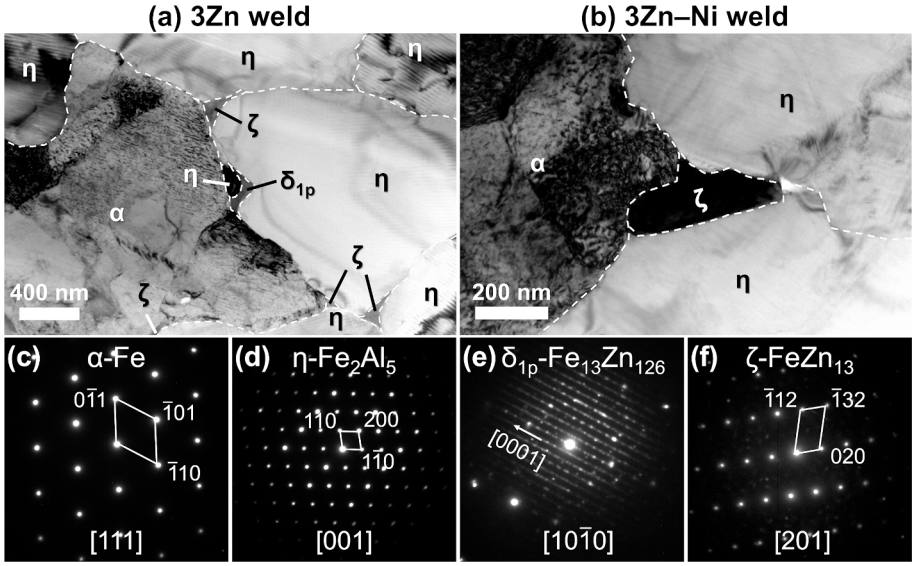

Fig. 8. BF-TEM images of the IMC layer of the (a) 3Zn and (b) 3Zn–Ni welds. The white dash lines in **a** and **b** indicate the phase and grain boundaries. SAED patterns of (c) α-Fe, (d) η-Fe_2Al_5, (e) δ_{1p}-$Fe_{13}Zn_{126}$, and (f) ζ-$FeZn_{13}$. The zone axis of SAED patterns is given at the bottom of each image.

weld strength.

To examine the softening mechanism of the IMC layer, cross-sectional TEM analyses were conducted on the IMC layers formed at the 3Zn and 3Zn–Ni weld interfaces. Note that the incident beam direction was nearly parallel to the growth direction of the η-Fe_2Al_5 layer, which was perpendicular to the weld interface. Fig. 7 shows the BF-STEM images and STEM-EDS maps of the inner IMC layers of each weld. For both welds, IMC layers primarily consist of η-Fe_2Al_5 and α-Fe. Notably, Zn maps show the Zn enrichment along the η/α interfaces, as indicated by white arrows.

BF-TEM images of the IMC layer of the 3Zn and 3Zn–Ni welds (Fig. 8**a and b**) and SAED patterns (Fig. 8**c–f**) reveal the formation of Fe–Zn IMCs, namely δ_{1p}-$Fe_{13}Zn_{126}$ (hexagonal, P63/mmc, a = b = 12.83 Å, c = 57.286 Å, γ = 120° [52]) and ζ-$FeZn_{13}$ (monoclinic, C2/m, a = 13.394 Å, b = 7.5980 Å, c = 5.066 Å, β = 127.23° [53]), in addition to α-Fe (cubic, Im-3 m, a = 2.866 Å [54]) and η-Fe_2Al_5. The SAED patterns obtained from different zone axes were used for accurate phase identification. These Fe–Zn IMCs, several hundred nanometers in size, are formed at interfaces involving at least one η grain, such as the η/α interface and η/η/α and η/η/η triple junctions. The SAED pattern of δ_{1p}-$Fe_{13}Zn_{126}$ along the [1010] zone axis (Fig. 8**e**) displays strong streaks parallel to the [0001] direction, which suggests the presence of stacking faults or micro-twins in a δ_{1p}-$Fe_{13}Zn_{126}$ grain. Further details of the structure and indexing of the spots are shown in Fig. 10**e**. The newly formed Fe–Zn IMCs were primarily the ζ-$FeZn_{13}$, with minor δ_{1p}-$Fe_{13}Zn_{126}$ in the 3Zn weld. However, in the 3Zn–Ni weld, only the ζ-$FeZn_{13}$ was identified. Remarkably, ζ-$FeZn_{13}$ and δ_{1p}-$Fe_{13}Zn_{126}$ are significantly softer than η-Fe_2Al_5, whose hardnesses were reported at 280–298 HV for ζ-$FeZn_{13}$ [55], 374–394 HV for δ_{1p}-$Fe_{13}Zn_{126}$ [55], and 1018 HV for η-Fe_2Al_5 [41]. Therefore, the formation of these softer Fe–Zn IMCs contributed to the softening of the IMC layer. The mechanisms of the further softening of the IMC layer by the combined addition of Zn and Ni are discussed later in this paper.

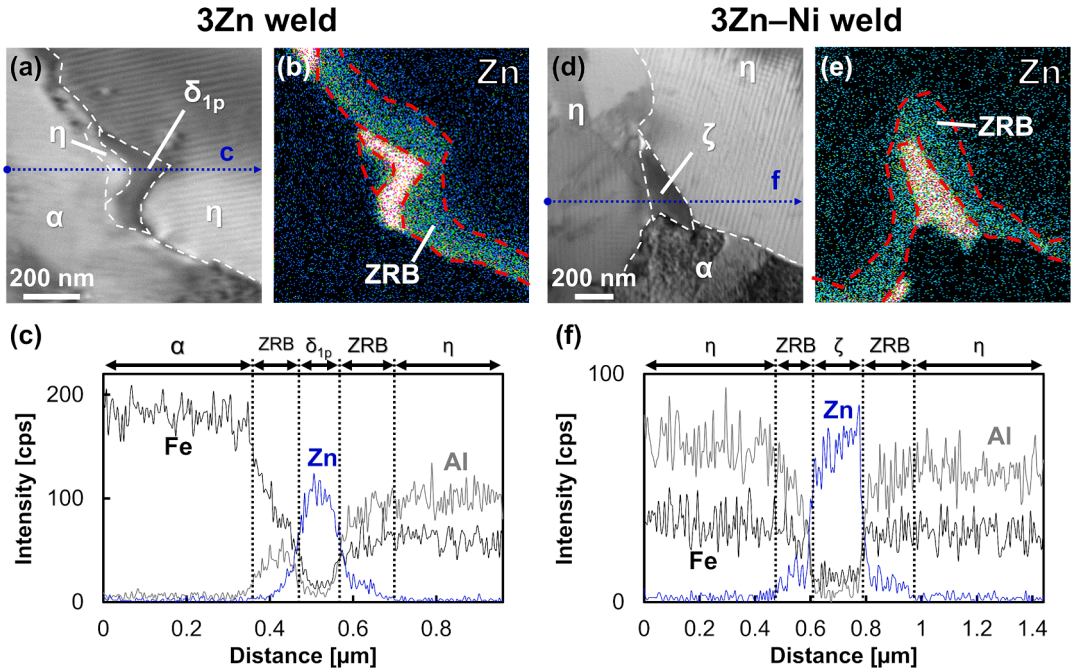

Fig. 9. STEM-EDS analyses of the Zn-rich zone formed along the η-Fe_2Al_5/α-Fe interface as indicated by white arrows in Zn maps in Fig. 7: (a, d) BF-STEM images of the area highlighted by the red squares in BF-STEM images in Fig. 7; (b, e) corresponding Zn maps; (c, f) EDS line analyses along the blue allows in **a** and **d**, showing that the Zn-rich zone consist of the Zn-rich band (ZRB) and Fe–Zn IMCs (δ_{1p}-$Fe_{13}Zn_{126}$ or ζ-$FeZn_{13}$).

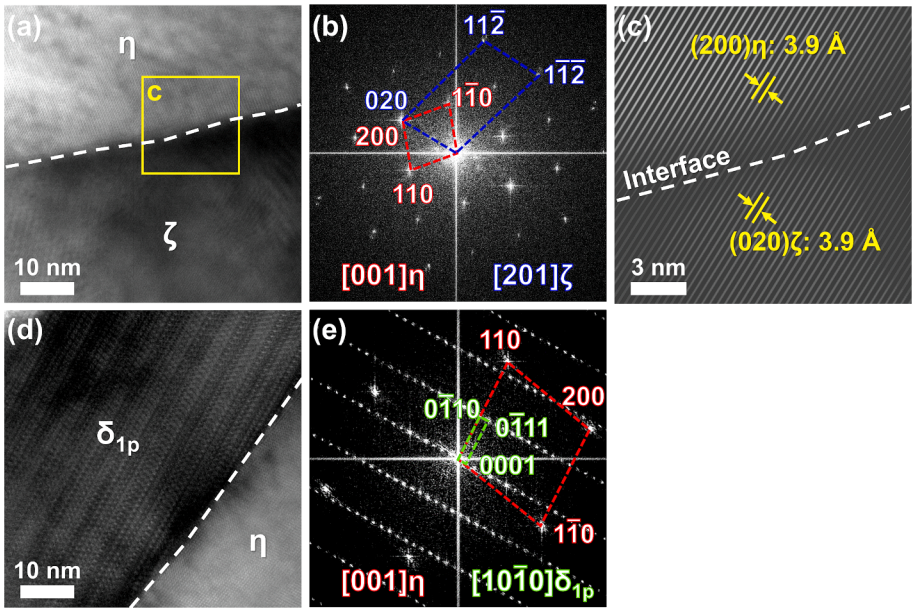

Fig. 10. HR-TEM observation results of the interfaces between each Fe–Zn IMC and η-Fe_2Al_5: (a) HRTEM image of a η-Fe_2Al_5/ζ-$FeZn_{13}$ interface; (b) corresponding FFT pattern, showing an orientation relationship of [001]η // [201]ζ and (200)η // (020)ζ; (c) IFFT image of the area highlighted by the yellow square in **a** derived from the (002)η and (020)ζ spots showing a coherent interface; (d) HRTEM image of a η-Fe_2Al_5/δ_{1p}-$Fe_{13}Zn_{126}$ interface; (e) corresponding FFT pattern, showing an orientation relationship of [001]η // [10$\bar{1}$0]δ_{1p} and (1$\bar{1}$0)η // (0110)δ_{1p}.

3.5. Formation mechanism of Fe–Zn IMCs

Fig. 9 presents the results of the STEM-EDS analyses of the Zn-rich zone, highlighted by the red squares in Fig. 7. Zn maps (**b** and **e**) and EDS line analyses across the Fe–Zn IMC (**c** and **f**) indicate that the Zn-rich zone consists of an Fe–Zn IMC and a Zn-rich band (ZRB). The ZRB, approximately 100–200 nm in width, is distributed along the η/α interface on the η-Fe_2Al_5 side. EDS line analyses suggest that the chemical composition of the ZRB is similar to η-Fe_2Al_5 containing Zn, and high-resolution transmission electron microscopy (HRTEM) validated that its crystal structure closely matched that of η-Fe_2Al_5. Additionally, EDS line analyses show that Zn is only detected in the ZRB, but not in bulk η-Fe_2Al_5 interior, implying that Zn diffused through the grain boundaries of η-Fe_2Al_5. The η grain boundaries serve as effective paths for Zn diffusion [42,56].

To examine the formation mechanisms of the Fe–Zn IMCs in detail, HRTEM was employed to observe the interfaces between each Fe–Zn IMC and η-Fe_2Al_5. Fig. 10**a–c** show the HRTEM observation results of a

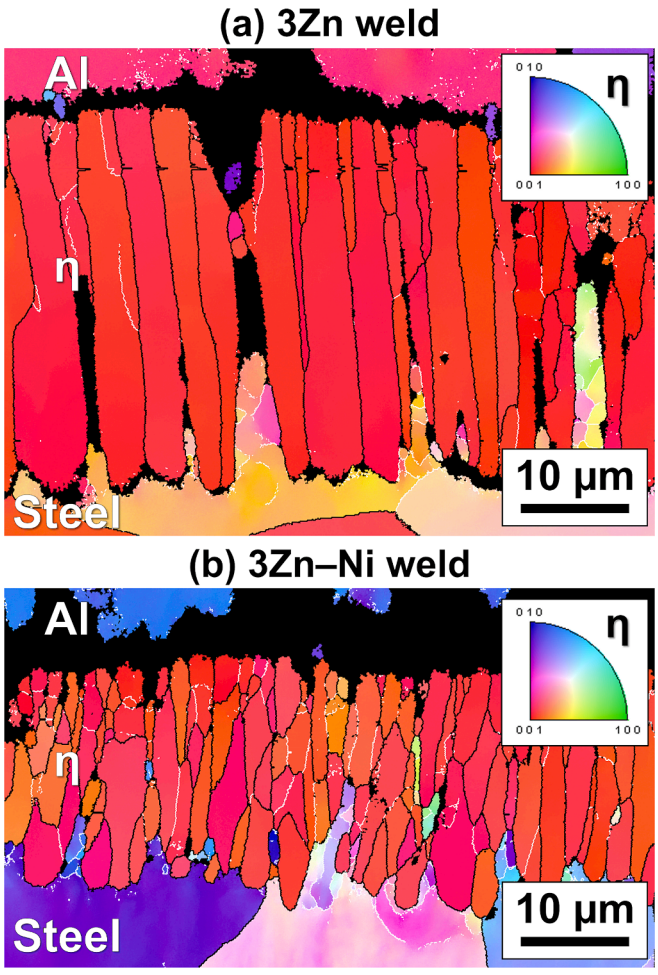

Fig. 11. EBSD IPF maps at the weld interfaces of the (a) 3Zn and (b) 3Zn–Ni welds. The orientation of η-Fe_2Al_5 along the direction perpendicular to the weld interface is shown by the color key inserted in the figure. High angle and low angle grain boundaries are shown by black and white lines, respectively.

η/ζ interface. Fig. 10**a** shows the HRTEM image of a η/ζ interface, and Fig. 10**b** shows a fast Fourier transform (FFT) pattern of the interface. Fig. 10**c** shows an inverse FFT (IFFT) image derived from the (200)η spot, which coincides with the (020)ζ spot. FFT analysis reveals that the orientation relationship between η-Fe_2Al_5 and ζ-$FeZn_{13}$ obeys [001]η // [201]ζ and (200)η // (020)ζ. The interplanar spacings of (200)η and (020)ζ, measured at both 3.9 Å by IFFT, which is in good agreement with the theoretical values of 3.828 Å [46] and 3.799 Å [53], respectively. The IFFT image of the η/ζ interface (Fig. 10**c**) indicates that there is no lattice mismatch between these IMCs, showing a perfectly coherent interface between them. To the best of our knowledge, this relationship has not yet been reported. Note that this orientation relationship and the coherent interface suggest the possibility of epitaxial growth of ζ-$FeZn_{13}$ on η-Fe_2Al_5. Fig. 10 presents the HRTEM observation results of a η/δ_{1p} interface. Fig. 10**d** shows an HRTEM image of a η/δ_{1p} interface, and Fig. 10**e** shows an FFT pattern of the interface. The HRTEM image reveals numerous stacking faults or micro-twins in the δ_{1p}-$Fe_{13}Zn_{126}$ grain, which is also indicated by streaks in the SAED pattern (Fig. 8**e**). FFT analysis exhibits the orientation relationship of [001]η // [1010]δ_{1p} and (1 1 0)η // (0110)δ_{1p}. Contrary to the η/ζ interface, there is a large lattice mismatch between δ_{1p}-$Fe_{13}Zn_{126}$ and η-Fe_2Al_5. It is believed that the stacking faults in δ_{1p}-$Fe_{13}Zn_{126}$ were introduced to accommodate the large lattice mismatch and the differences in lattice parameters during the phase transformation from η-Fe_2Al_5 to δ_{1p}-$Fe_{13}Zn_{126}$.

3.6. *Effect of subsequent Ni addition on IMC softening*

As aforementioned, the combined addition of Zn and Ni softened the IMC layer more effectively than the addition of Zn alone, thereby improving the weld strength. The softening mechanism is explained as follows: Fig. 11 presents the EBSD inverse pole figure (IPF) maps at the weld interfaces of the 3Zn and 3Zn–Ni welds. In the IPF maps, θ-Fe_4Al_{13} layer formed at the Al/η interface was hardly imaged because the sample surface preparation was optimized for the η-Fe_2Al_5. IPF maps show the grain morphology of η-Fe_2Al_5: η-Fe_2Al_5 layer of the 3Zn weld primarily consists of coarse columnar grains, while the η-Fe_2Al_5 grains are noticeably finer in the 3Zn–Ni welds, indicating an increase of η-Fe_2Al_5 grain boundaries. The average widths of the η-Fe_2Al_5 grains, measured by the line intercept method from several IPF maps, were 2.2 ± 0.3 μm for the 3Zn weld and 1.4 ± 0.1 μm for the 3Zn–Ni weld, respectively. This result highlighted the grain refinement of η-Fe_2Al_5 via Ni addition

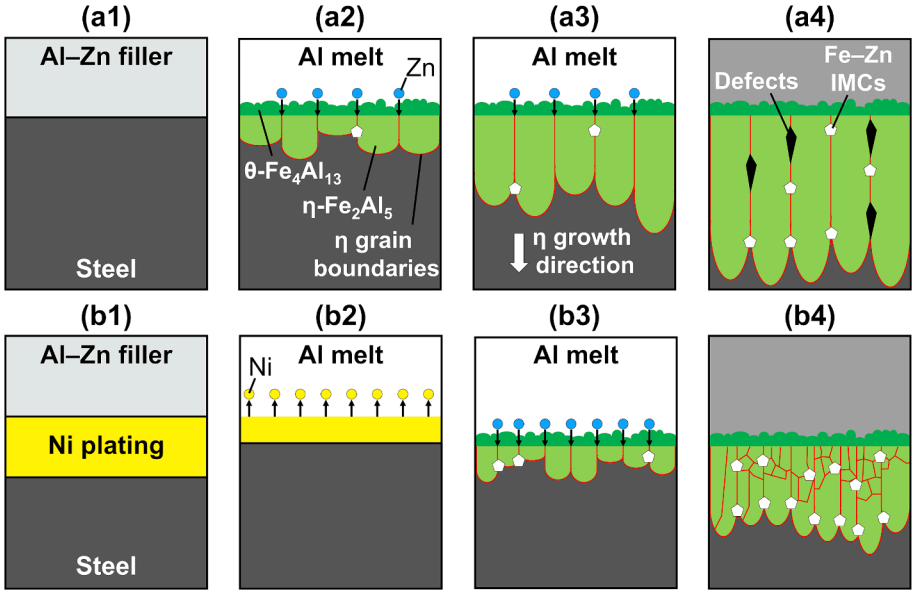

Fig. 12. Schematic of the evolution of the IMC layer of (a1–a4) Zn and (b1–b4) Zn–Ni welds: (a1, b1) before the brazing process; (a2, b2) at the initial stage of the brazing process; (a3, b3) growth of the IMC layer; (a4, b4) resulting microstructure of the IMC layer.

[38] even with Zn, though the mechanism of grain refinement is not clarified. The detailed investigation on the mechanism is ongoing and will be reported in separate papers in the future. As previously noted, η-Fe_2Al_5 grain boundaries serve as rapid diffusion pathways for Zn. Additionally, interfaces involving one or more η-Fe_2Al_5 grains act as formation sites for the Fe–Zn IMCs. Therefore, the addition of Ni, refining the η-Fe_2Al_5 grain, was believed to enhance Zn diffusion into the η-Fe_2Al_5 layer from the Al melt and promote the formation of the Fe–Zn IMCs, resulting in the further softening of the IMC layer. The SEM-WDS analysis showed that the average Zn content in the IMC layer was slightly high in the 3Zn–Ni weld (0.34 ± 0.03 at.%) compared to the 3Zn weld (0.22 ± 0.02 at.%), suggesting that the IMC layer in the 3Zn–Ni weld contained more Fe–Zn IMCs than the 3Zn weld.

3.7. Mechanism of IMC formation and strengthening weld

Fig. 12 illustrates the effects of the combined addition of Zn and Ni on the formation of the IMC layer based on the experimental results. Initially, in Zn welds, a contact between liquid-Al and steel resulted in the formation of the η-Fe_2Al_5 and θ-Fe_4Al_{13} layers. Notably, the η-Fe_2Al_5 layer is formed as the primary IMC due to its rapid growth rate [57,58] (**a2**). Subsequently, Zn diffused from the Al melt through η-Fe_2Al_5 grain boundaries, forming Fe–Zn IMCs at specific sites. In contrast, Ni plating in Zn–Ni welds initially prevented direct contact between liquid-Al and steel, delaying the formation of the IMCs (**b2**). As the brazing process progressed, once the Ni plating was removed, a liquid Al/solid Fe reaction occurred. In Zn–Ni welds, Zn diffusion and the formation of Fe–Zn IMCs were promoted due to the η-Fe_2Al_5 grain refinement via Ni [38] (**b3**). The resulting microstructures of the IMC layers in the welds are drawn in **a4** and **b4**. The IMC layer of the Zn–Ni welds was thinner than that of the Zn welds (Fig. 6) because the Ni plating reduced the reaction time between the liquid Al and steel. This reduction in the thickness of the IMC layer partially contributed to the improvement in the weld strength. Additionally, Ni plating decreased the number of defects in the η-Fe_2Al_5 layer by suppressing Zn evaporation, which also contributed to the improvement in the weld strength. Nanoindentation tests revealed that the hardness of the IMC layer of the Zn–Ni weld was lower than that of the Zn weld, suggesting that more Fe–Zn IMCs were formed in the Zn–Ni welds than in the Zn welds. Further softening of the IMC layer is believed to significantly improve the weld strength.

4. Conclusion

In this study, the effects of Zn and Ni on the weld strength and microstructure of the IMC layer in AA5052 and LCS dissimilar welds were examined. The weld strength was significantly improved from 41 to 120 MPa by the combined addition of Zn and Ni. The combined addition resulted in the softening of the IMC layer owing to the formation of Fe–Zn IMCs, suppression of defect formation in the IMC layer, and a reduction in the thickness of the IMC layer, significantly improving the weld strength.

CRediT authorship contribution statement

Kiyoaki T. Suzuki: Writing – original draft, Visualization, Investigation, Formal analysis, Data curation. **Shun Omura:** Writing – review & editing, Data curation. **Shun Tokita:** Writing – review & editing, Data curation. **Yujiro Tatsumi:** Resources. **Sylvain Dancette:** Writing – review & editing. **Yutaka S. Sato:** Writing – review & editing, Validation, Resources, Project administration, Funding acquisition, Data curation, Conceptualization.

Declaration of competing interest

The authors declare that they have no known competing financial interests or personal relationships that could have appeared to influence the work reported in this paper.

Data availability

Data will be made available on request.

Acknowledgements

The authors thank Dr. Kosei Kobayashi for the technical assistance. This study was partially supported by the Graduate Program of Materials Science at Tohoku University, JSPS KAKENHI, Grant Number 21H01662, and JST SPRING, Grant Number JPMJSP2114.

References

[1] Y. Ruan, N. Yan, H.Z. Zhu, K. Zhou, B. Wei, Thermal performance determination of binary Fe-Al alloys at elevated temperatures, J. Alloy. Compd. 701 (2017) 676–681, https://doi.org/10.1016/j.jallcom.2017.01.131.
[2] N. Jimenez-Mena, A. Simar, P.J. Jacques, On the interplay between intermetallic controlled growth and hot tearing susceptibility in Al-to-steel welding with additional interlayers, Mater. Des. 180 (2019) 107958, https://doi.org/10.1016/j.matdes.2019.107958.
[3] U.F.H. Suhuddin, V. Fischer, A. Kostka, J.F. dos Santos, Microstructure evolution in refill friction stir spot weld of a dissimilar Al–Mg alloy to Zn-coated steel, Sci. Technol. Weld. Join. 22 (2017) 658–665, https://doi.org/10.1080/13621718.2017.1300744.
[4] T. Bergh, S.M. Arbo, A.B. Hagen, J. Blindheim, J. Friis, M.Z. Khalid, I.G. Ringdalen, R. Holmestad, I. Westermann, P.E. Vullum, On intermetallic phases formed during interdiffusion between aluminium alloys and stainless steel, Intermetallics 142 (2022) 107443, https://doi.org/10.1016/j.intermet.2021.107443.
[5] L. Shi, J. Kang, C. Qian, J. Liang, B. Shalchi-Amirkhiz, A.S. Haselhuhn, B. E. Carlson, Role of Fe2Al5 in fracture of novel dissimilar aluminum-steel resistance spot welds using multi-ring domed electrodes, Mater. Sci. Eng. A 831 (2022) 142233, https://doi.org/10.1016/j.msea.2021.142233.
[6] T. Sapanathan, N. Jimenez-Mena, I. Sabirov, M.A. Monclús, J.M. Molina-Aldareguía, P. Xia, L. Zhao, A. Simar, A new physical simulation tool to predict the interface of dissimilar aluminum to steel welds performed by friction melt bonding, J. Mater. Sci. Technol. 35 (2019) 2048–2057, https://doi.org/10.1016/j.jmst.2019.05.004.
[7] B. Lemmens, H. Springer, M.J. Duarte, I. De Graeve, J. De Strycker, D. Raabe, K. Verbeken, Atom probe tomography of intermetallic phases and interfaces formed in dissimilar joining between Al alloys and steel, Mater. Charact. 120 (2016) 268–272, https://doi.org/10.1016/j.matchar.2016.09.008.
[8] P. Huilgol, K.R. Udupa, K.U. Bhat, Metastable microstructures at the interface between AISI 321 steel and molten aluminum during hot-dip aluminizing, Surf. Coat. Technol. 348 (2018) 22–30, https://doi.org/10.1016/j.surfcoat.2018.05.013.
[9] Z. Que, C. Fang, C.L. Mendis, Y. Wang, Z. Fan, Effects of Si solution in θ-Al13Fe4 on phase transformation between Fe-containing intermetallic compounds in Al alloys, J. Alloy. Compd. 932 (2023) 167587, https://doi.org/10.1016/j.jallcom.2022.167587.
[10] C. Chatelier, K. Anand, P. Gille, M.-C. De Weerd, J. Ledieu, V. Fournée, A. Resta, A. Vlad, Y. Garreau, A. Coati, É. Gaudry, Revealing the epitaxial interface between $Al_{13}Fe_4$ and Al_5Fe_2 enabling atomic Al interdiffusion, ACS Appl. Mater. Interfaces 15 (2023) 19593–19603, https://doi.org/10.1021/acsami.2c22886.
[11] C. Zhang, M. Wu, J. Pu, Q. Shan, Y. Sun, S. Wang, S.K.U.G. Hermann, Effect of Cu coating on microstructure and properties of Al/steel welding-brazing joints obtained by cold metal transfer (CMT), Coatings 12 (2022) 1123, https://doi.org/10.3390/coatings12081123.
[12] D. Wallerstein, E.L. Solla, F. Lusquiños, R. Comesaña, J. Del Val, A. Riveiro, J. Pou, Advanced characterization of intermetallic compounds in dissimilar aluminum-steel joints obtained by laser welding-brazing with Al–Si filler metals, Mater. Charact. 179 (2021) 111345, https://doi.org/10.1016/j.matchar.2021.111345.
[13] W. Ratanathavorn, A. Melander, H. Magnusson, Intermetallic compounds in friction stirred lap joints between AA5754/galvanised ultra-high strength steel, Sci. Technol. Weld. Join. 21 (2016) 653–659, https://doi.org/10.1080/13621718.2016.1163878.
[14] W. Ratanathavorn, A. Melander, Influence of zinc on intermetallic compounds formed in friction stir welding of AA5754 aluminium alloy to galvanised ultra-high strength steel, Sci. Technol. Weld. Join. 22 (2017) 673–680, https://doi.org/10.1080/13621718.2017.1302553.
[15] M. Zhao, X. Wang, S. Tang, Z. Lin, H. Chen, Determination and characterization of heat input, microstructure and performance in cold metal transfer weld-brazing of dissimilar AA6061-T6 to SS304 sheets, Trans. Indian Inst. Met. (2023), https://doi.org/10.1007/s12666-022-02796-y.
[16] P. Xu, X. Hua, C. Shen, G. Mou, Y. Huang, K. Wu, Y. Zhang, F. Li, Fracture mode variation mechanism of Al/steel dissimilar overlap joint made using variable polarity cold metal transfer-based arc brazing, J. Mater. Eng. Perform. 32 (2023) 512–523, https://doi.org/10.1007/s11665-022-07134-3.
[17] W. Xu, H. He, Y. Yi, H. Wang, C. Yu, W. Fang, Dissimilar joining of stainless steel and aluminum using twin-wire CMT, Weld. World 65 (2021) 1541–1551, https://doi.org/10.1007/s40194-021-01089-0.

[18] M. Zheng, J. Yang, J. Xu, J. Jiang, H. Zhang, J.P. Oliveira, X. Lv, J. Xue, Z. Li, Interfacial microstructure and strengthening mechanism of dissimilar laser al/steel joint via a porous high entropy alloy coating, J. Mater. Res. Technol. 23 (2023) 3997–4011, https://doi.org/10.1016/j.jmrt.2023.02.040.
[19] J. Xie, C. Cai, B. Zhang, J. Yu, Y. Liu, H. Chen, Microstructure evolution and fracture behavior of rotating laser welded-brazed 6061 aluminum alloys/304 SS dissimilar joint, Mater. Charact. 195 (2023) 112543, https://doi.org/10.1016/j.matchar.2022.112543.
[20] H.R. Javadinejad, M. Lee, C.H. Shim, H.J. Chang, J.H. Kim, Interfacial reaction mechanism during laser brazing of Zn–Mg–Al-coated steel to AA 6061 aluminum alloy, J. Manuf. Process. 83 (2022) 471–487, https://doi.org/10.1016/j.jmapro.2022.09.013.
[21] R. Beygi, R.J.C. Carbas, A.Q. Barbosa, E.A.S. Marques, L.F.M. da Silva, Buttering for FSW: enhancing the fracture toughness of Al-Fe intermetallics through nanocrystallinity and suppressing their growth, J. Manuf. Process. 90 (2023) 233–241, https://doi.org/10.1016/j.jmapro.2023.02.001.
[22] M. Zhang, Y.D. Wang, P. Xue, H. Zhang, D.R. Ni, K.S. Wang, Z.Y. Ma, High-quality dissimilar friction stir welding of Al to steel with no contacting between tool and steel plate, Mater. Charact. 191 (2022) 112128, https://doi.org/10.1016/j.matchar.2022.112128.
[23] T. Zhang, K. Wang, K. Qiao, B. Wu, Q. Liu, P. Han, W. Wang, Y. Wang, Z. Hao, P. Zheng, Evolution mechanism of intermetallic compounds and the mechanical properties of dissimilar friction stir welded QP980 steel and 6061 aluminum alloy, Mater. Charact. 202 (2023) 113033, https://doi.org/10.1016/j.matchar.2023.113033.
[24] X. Wang, Y. Morisada, H. Fujii, High-strength Fe/Al dissimilar joint with uniform nanometer-sized intermetallic compound layer and mechanical interlock formed by adjustable probes during double-sided friction stir spot welding, Mater. Sci. Eng. A 809 (2021) 141005, https://doi.org/10.1016/j.msea.2021.141005.
[25] Y.F. Sun, H. Fujii, N. Takaki, Y. Okitsu, Microstructure and mechanical properties of dissimilar Al alloy/steel joints prepared by a flat spot friction stir welding technique, Mater. Des. 47 (2013) 350–357, https://doi.org/10.1016/j.matdes.2012.12.007.
[26] J.-Y. Lin, S. Nambu, T. Koseki, Evolution of bonding interface during ultrasonic welding between steel and aluminium alloy, Sci. Technol. Weld. Join. 24 (2019) 83–91, https://doi.org/10.1080/13621718.2018.1491376.
[27] L. Xu, L. Wang, Y.-C. Chen, J.D. Robson, P.B. Prangnell, Effect of interfacial reaction on the mechanical performance of steel to aluminum dissimilar ultrasonic spot welds, Metall. Mater. Trans. A 47 (2016) 334–346, https://doi.org/10.1007/s11661-015-3179-7.
[28] F. Haddadi, Rapid intermetallic growth under high strain rate deformation during high power ultrasonic spot welding of aluminium to steel, Mater. Des. 66 (2015) 459–472, https://doi.org/10.1016/j.matdes.2014.07.001.
[29] N. Zhang, Q. Hu, F. Yang, W. Lu, Z. Ding, S. Cao, L. Yu, X. Ge, J. Li, Effect of Si on the growth behavior of the Fe2Al5 phase at Al-xSi(liquid)/Fe(solid) interface during holding by in-situ synchrotron radiography, Metall. Mater. Trans. A 51 (2020) 2711–2718, https://doi.org/10.1007/s11661-020-05754-9.
[30] T. Wang, C. Chen, J. Ma, S. Wei, M. Xiong, F. Mao, P. Zhang, G. Zhang, Influence of Si on the intermetallic compound formation in the hot-dipped aluminide medium carbon steel, Mater. Charact. 197 (2023) 112700, https://doi.org/10.1016/j.matchar.2023.112700.
[31] B. Lemmens, H. Springer, I. De Graeve, J. De Strycker, D. Raabe, K. Verbeken, Effect of silicon on the microstructure and growth kinetics of intermetallic phases formed during hot-dip aluminizing of ferritic steel, Surf. Coat. Technol. 319 (2017) 104–109, https://doi.org/10.1016/j.surfcoat.2017.03.040.
[32] B. Dangi, T.W. Brown, K.N. Kulkarni, Effect of silicon, manganese and nickel present in iron on the intermetallic growth at iron - aluminum alloy interface, J. Alloy. Compd. 769 (2018) 777–787, https://doi.org/10.1016/j.jallcom.2018.07.364.
[33] H. Springer, A. Kostka, E.J. Payton, D. Raabe, A. Kaysser-Pyzalla, G. Eggeler, On the formation and growth of intermetallic phases during interdiffusion between low-carbon steel and aluminum alloys, Acta Mater. 59 (2011) 1586–1600, https://doi.org/10.1016/j.actamat.2010.11.023.
[34] H. Azimaee, M. Sarfaraz, M. Mirjalili, K. Aminian, Effect of silicon and manganese on the kinetics and morphology of the intermetallic layer growth during hot-dip aluminizing, Surf. Coat. Technol. 357 (2019) 483–496, https://doi.org/10.1016/j.surfcoat.2018.10.035.
[35] Y. Su, X. Hua, Y. Wu, Influence of alloy elements on microstructure and mechanical property of aluminum–steel lap joint made by gas metal arc welding, J. Mater. Process. Technol. 214 (2014) 750–755, https://doi.org/10.1016/j.jmatprotec.2013.11.022.
[36] H. Xia, X. Zhao, C. Tan, B. Chen, X. Song, L. Li, Effect of Si content on the interfacial reactions in laser welded-brazed Al/steel dissimilar butted joint, J. Mater. Process. Technol. 258 (2018) 9–21, https://doi.org/10.1016/j.jmatprotec.2018.03.010.
[37] W.-J. Cheng, C.-J. Wang, Effect of silicon on the formation of intermetallic phases in aluminide coating on mild steel, Intermetallics 19 (2011) 1455–1460, https://doi.org/10.1016/j.intermet.2011.05.013.
[38] H.S. Furuya, Y.T. Sato, Y.S. Sato, H. Kokawa, Y. Tatsumi, Strength improvement through grain refinement of intermetallic compound at Al/Fe dissimilar joint interface by the addition of alloying elements, Metall. Mater. Trans. A 49 (2018) 527–536, https://doi.org/10.1007/s11661-017-4442-x.
[39] K.T. Suzuki, S. Omura, S. Tokita, Y.S. Sato, Y. Tatsumi, Drastic improvement in dissimilar aluminum-to-steel joint strength by combining positive roles of silicon and nickel additions, Mater. Des. 225 (2023) 111444, https://doi.org/10.1016/j.matdes.2022.111444.
[40] G. Qin, Z. Ao, Y. Chen, C. Zhang, P. Geng, Formability behavior of Al/steel MIG arc brazed-fusion welded joint, J. Mater. Process. Technol. 273 (2019) 116255, https://doi.org/10.1016/j.jmatprotec.2019.116255.
[41] J. Yang, Y.L. Li, H. Zhang, W. Guo, Y. Zhou, Control of interfacial intermetallic compounds in Fe–Al joining by Zn addition, Mater. Sci. Eng. A 645 (2015) 323–327, https://doi.org/10.1016/j.msea.2015.08.036.
[42] Y. Ma, H. Dong, P. Li, B. Wu, W. Wu, W. Qian, B. Wang, Control of various Zn-based weld seam/steel interface structures in AA5083/FH36 steel welded joint, Mater. Des. 230 (2023) 111971, https://doi.org/10.1016/j.matdes.2023.111971.
[43] H. He, L. Zhang, Z. Liu, W. Zhao, Evolution of intermetallics between solid Fe-Cr/Fe-Ni alloys and molten aluminium, Int. J. Mech. Sci. 257 (2023) 108549, https://doi.org/10.1016/j.ijmecsci.2023.108549.
[44] Q. Luo, W. Liu, W. Li, Q. Gu, B. Wang, Q. Li, Revisiting selective nucleation at heterophase interfaces in Fe–Al solid-liquid reaction, J. Mater. Res. Technol. 17 (2022) 452–458, https://doi.org/10.1016/j.jmrt.2022.01.036.
[45] A. Griger, V. Stefániay, T. Turmezey, Crystallographic data and chemical compositions of aluminium-rich Al-Fe intermetallic phases, Int. J. Mater. Res. 77 (1986) 30–35, https://doi.org/10.1515/ijmr-1986-770107.
[46] U. Burkhardt, Y. Grin, M. Ellner, K. Peters, Structure refinement of the iron–aluminium phase with the approximate composition Fe2Al5, Acta Crystallogr. B 50 (1994) 313–316, https://doi.org/10.1107/S0108768193013989.
[47] C. Dharmendra, K.P. Rao, J. Wilden, S. Reich, Study on laser welding–brazing of zinc coated steel to aluminum alloy with a zinc based filler, Mater. Sci. Eng. A 528 (2011) 1497–1503, https://doi.org/10.1016/j.msea.2010.10.050.
[48] H. Springer, A. Szczepaniak, D. Raabe, On the role of zinc on the formation and growth of intermetallic phases during interdiffusion between steel and aluminium alloys, Acta Mater. 96 (2015) 203–211, https://doi.org/10.1016/j.actamat.2015.06.028.
[49] X. Zhang, K. Gao, Z. Wang, X. Hu, J. Wang, Z. Nie, In Situ SEM, TEM, EBSD characterization of nucleation and early growth of pure Fe/Pure Al intermetallic compounds, Materials 16 (2023) 6022, https://doi.org/10.3390/ma16176022.
[50] X. Cao, J. Duan, Z. Li, B. Chang, C. Xu, Z. Xie, An investigation on laser/DP-MIG hybrid weldability of aluminum to Al-Si coated boron steel, Opt. Laser Technol. 150 (2022) 107939, https://doi.org/10.1016/j.optlastec.2022.107939.
[51] J. Rong, Z. Kang, S. Chen, D. Yang, J. Huang, J. Yang, Growth kinetics and thickness prediction of interfacial intermetallic compounds between solid steel and molten aluminum based on thermophysical simulation in a few seconds, Mater. Charact. 132 (2017) 413–421, https://doi.org/10.1016/j.matchar.2017.09.012.
[52] N.L. Okamoto, K. Tanaka, A. Yasuhara, H. Inui, Structure refinement of the δ1p phase in the Fe–Zn system by single-crystal X-ray diffraction combined with scanning transmission electron microscopy, Acta Crystallogr. Sect. B Struct. Sci. Cryst. Eng. Mater. 70 (2014) 275–282, https://doi.org/10.1107/S2052520613034410.
[53] R. Belin, L. Monconduit, M. Tillard, Redetermination of the iron–zinc phase FeZn13, Acta Crystallogr. C 56 (2000) 267–268, https://doi.org/10.1107/S0108270199014997.
[54] E.P. Yelsukov, E.V. Voronina, V.A. Barinov, Mössbauer study of magnetic properties formation in disordered Fe-Al alloys, J. Magn. Magn. Mater. 115 (1992) 271–280, https://doi.org/10.1016/0304-8853(92)90069-Z.
[55] K. Han, I. Lee, I. Ohnuma, K. Okuda, R. Kainuma, Micro-vickers hardness of intermetallic compounds in the Zn-rich portion of Zn–Fe binary system, ISIJ Int. 58 (2018) 1578–1583, https://doi.org/10.2355/isijinternational.ISIJINT-2018-111.
[56] Y. Adachi, M. Arai, Transformation of Fe–Al phase to Fe–Zn phase on pure iron during galvanizing, Mater. Sci. Eng. A 254 (1998) 305–310, https://doi.org/10.1016/S0921-5093(97)00840-X.
[57] Z. Ding, Q. Hu, W. Lu, X. Ge, S. Cao, S. Sun, T. Yang, M. Xia, J. Li, Microstructural evolution and growth behavior of intermetallic compounds at the liquid Al/solid Fe interface by synchrotron X-ray radiography, Mater. Charact. 136 (2018) 157–164, https://doi.org/10.1016/j.matchar.2017.12.024.
[58] Y. Wang, Y. Liu, H. Pan, J. Hou, H. Mao, B. Liu, H. Xu, P. Bai, R.D.K. Misra, Phase formation and mechanical properties of iron-based intermetallic/steel laminate composites, Adv. Compos. Hybrid Mater. 5 (2022) 2171–2183, https://doi.org/10.1007/s42114-021-00264-7.